AGU PUBLICATIONS

Geophysical Research Letters

RESEARCH LETTER
10.1002/2016GL068083

Key Points:
- We conduct a joint analysis of receiver functions and 3-D CMT solutions for the 2015 Gorkha sequence to explore the geometry of the MHT
- Results outline the ramp-flat-ramp geometry of the MHT and show that the flat seismogenic portion of the MHT is confined within a LVZ
- The frequency-dependent behavior of the Gorkha rupture can be explained by a downdip fault kink and the presence of fluids in the LVZ

Supporting Information:
- Supporting Information S1

Correspondence to:
Z. Duputel,
zacharie.duputel@unistra.fr

Citation:
Duputel, Z., J. Vergne, L. Rivera, G. Wittlinger, V. Farra, and G. Hetényi (2016), The 2015 Gorkha earthquake: A large event illuminating the Main Himalayan Thrust fault, *Geophys. Res. Lett.*, *43*, doi:10.1002/2016GL068083.

Received 2 FEB 2016
Accepted 1 MAR 2016
Accepted article online 7 MAR 2016

The 2015 Gorkha earthquake: A large event illuminating the Main Himalayan Thrust fault

Zacharie Duputel[1], Jérôme Vergne[1], Luis Rivera[1], Gérard Wittlinger[1], Véronique Farra[2], and György Hetényi[3]

[1]IPGS-EOST, CNRS/Université de Strasbourg, Strasbourg, France, [2]Institut de Physique du Globe de Paris, Paris, France, [3]Institute of Earth Sciences, University of Lausanne, Lausanne, Switzerland

Abstract The 2015 Gorkha earthquake sequence provides an outstanding opportunity to better characterize the geometry of the Main Himalayan Thrust (MHT). To overcome limitations due to unaccounted lateral heterogeneities, we perform Centroid Moment Tensor inversions in a 3-D Earth model for the main shock and largest aftershocks. In parallel, we recompute *S*-to-*P* and *P*-to-*S* receiver functions from the Hi-CLIMB data set. Inverted centroid locations fall within a low-velocity zone at 10–15 km depth and corresponding to the subhorizontal portion of the MHT that ruptured during the Gorkha earthquake. North of the main shock hypocenter, receiver functions indicate a north dipping feature that likely corresponds to the midcrustal ramp connecting the flat portion to the deep part of the MHT. Our analysis of the main shock indicates that long-period energy emanated updip of high-frequency radiation sources previously inferred. This frequency-dependent rupture process might be explained by different factors such as fault geometry and the presence of fluids.

1. Introduction

The Main Himalayan Thrust (MHT) is one of the largest and fastest-slipping continental megathrust on Earth. It absorbs most of the convergence between India and southern Tibet and represents the largest source of seismic hazard in Nepal and North India (Figure 1) [*Ader et al.*, 2012]. The largest instrumentally recorded earthquake in this region is the $M = 8.2$ 1934 Bihar earthquake shown in Figure 1, which propagated up to the front of the Himalaya where the MHT emerges at the surface [*Geller and Kanamori*, 1977; *Sapkota et al.*, 2013] as the Main Frontal Thrust (MFT). From paleoseismological studies, historical events in 1255 and 1505 might have also ruptured the MHT and reached the surface [*Sapkota et al.*, 2013; *Bollinger et al.*, 2014]. Other large earthquakes affected the area of Kathmandu in 1344 and 1833 but whether they occurred on the MHT is debated [*Bilham*, 1995; *Bollinger et al.*, 2014].

The geometry of the MHT has been investigated through various geological and geophysical field campaigns [*Brunel*, 1986; *Zhao et al.*, 1993; *Brown et al.*, 1996; *Hauck et al.*, 1998; *Lemonnier et al.*, 1999; *Lavé and Avouac*, 2001; *Nabelek et al.*, 2009; *Wittlinger et al.*, 2009; *Schulte-Pelkum et al.*, 2005; *Caldwell et al.*, 2013]. Among them, analysis of receiver functions (RF) from the Hi-CLIMB (Himalayan-Tibetan Continental Lithosphere during Mountain Building) experiment reveals a low-velocity zone (LVZ) extending from the Lesser Himalayas to southern Tibet and interpreted as the signature of the MHT beneath Lesser and Higher Himalayas [*Nabelek et al.*, 2009]. Below Nepal this LVZ appears almost horizontal and located at 10 to 15 km depth [*Nabelek et al.*, 2009], but the horizontal and vertical resolutions are limited by the smoothing of the migrated cross section and the frequency range used to produce the receiver functions. Moreover, because of large depth uncertainties in previous earthquake catalogs, the depth of the MHT relative to the LVZ is still unclear [*Nabelek et al.*, 2009; *Caldwell et al.*, 2013]. Between the Lesser and Higher Himalayas, debate is still ongoing regarding the presence of a midcrustal ramp along the MHT at the front of the Higher Himalayas [*Lavé and Avouac*, 2001; *Bollinger et al.*, 2004; *Wobus et al.*, 2005; *Elliott et al.*, 2016].

On 25 April 2015, a large $M_w = 7.8$ earthquake occurred close to Kathmandu (28.230°N, 84.731°E, 06:11:25 UTC; U.S. Geological Survey (USGS) National Earthquake Information Center: http://earthquake.usgs.gov). This event was followed by a $M_w = 7.2$ aftershock on 12 May 2015. *W* phase inversion was performed both for the main shock and the largest aftershock (Figure S1 in the supporting information). The *W* phase moment tensor estimates are similar to global centroid moment tensor (GCMT) solutions, and the northward low-dipping planes suggest that both events ruptured the MHT. However, centroid depth estimates vary significantly between the different catalogs; *W* phase and SCARDEC (Seismic source characteristics retrieved from deconvolvolving

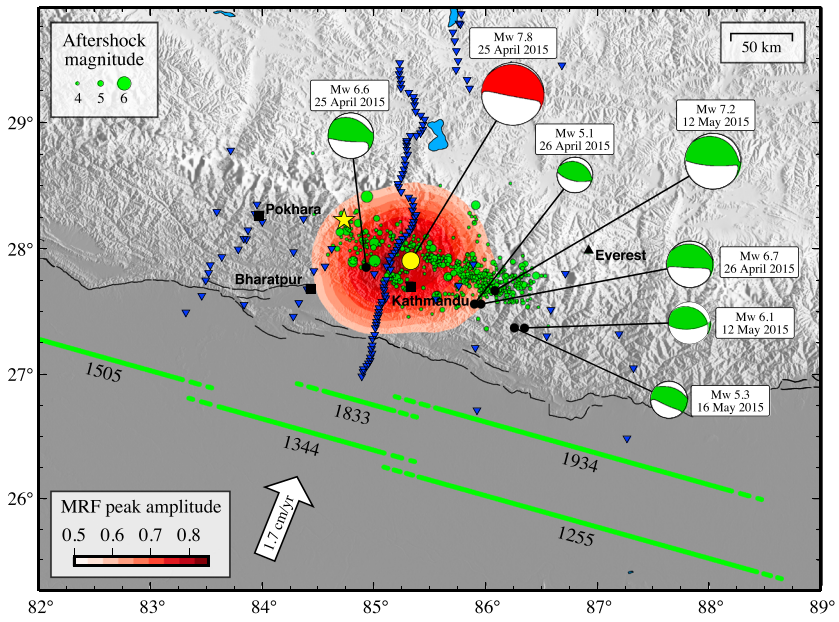

Figure 1. The 2015 Nepal earthquake sequence. Centroid moment tensor (CMT) inversions are conducted using body waves and surface waves assuming a 3-D Earth model. The red focal mechanism is the CMT solution obtained for the $M_w = 7.8$ main shock. Yellow circle is the corresponding centroid location, and yellow star is the USGS hypocenter. Green focal mechanisms are solutions obtained for $M_w \geq 5$ aftershocks. Red colors indicate peak-stacked amplitude in the source region from moment rate functions (MRF) backprojected relative to the main shock epicentral location. Green lines indicate the supposed rupture zones for the 1255, 1344, 1505, 1833, and 1934 earthquakes. Green circles are aftershocks of magnitude $M \geq 4$ from *Adhikari et al.* [2015] (2015/04/25 to 2015/06/07).

teleseismic body waves) yield to depths larger than 20 km (http://wphase.unistra.fr, http://geoscope.ipgp.fr), while GCMT converges to its minimum allowed depth of 12 km [*Ekström et al.*, 2012]. On the other hand, preliminary finite-fault inversions [*Avouac et al.*, 2015; *Galetzka et al.*, 2015; *Grandin et al.*, 2015; *Yagi and Okuwaki*, 2015] fixed the hypocentral depth to ~15 km according to the USGS preliminary determined hypocenter location, which was later updated to 8.2 km (http://geoscope.ipgp.fr).

The 2015 Gorkha earthquake sequence offers an outstanding occasion to better constrain and resolve the geometry of the MHT. We exploit global long-period data to perform centroid moment tensor (CMT) inversion in a 3-D Earth model. This new CMT approach enables more accurate centroid depth estimates and is accompanied by a detailed directivity analysis of apparent moment rate functions. In parallel, we reprocessed both *S*-to-*P* and *P*-to-*S* receiver functions under Nepal using a selection of teleseismic events with $M_w > 6$ recorded by the Hi-CLIMB broadband network. The low-dip angle of the MHT (optimum for receiver function imaging) and the coincidence of having the deployment of Hi-CLIMB stations above the Gorkha rupture area is a rare opportunity to image a fault that ruptured in a large earthquake.

2. Depth and Geometry of the Main Himalayan Thrust

As discussed above, the centroid depths of the 2015 Gorkha earthquake sequence are uncertain. The quality of centroid depth estimates depends on many factors like the size of the event, the azimuthal coverage, and the type of used data (*W* phase, body waves, mantle waves, and surface waves). The inaccuracy of Earth models used for Green's function calculation is a major source of uncertainty in source inversions [*Nakanishi and Kanamori*, 1982; *Smith and Ekström*, 1996; *Duputel et al.*, 2014]. The *W* phase approach is based on a 1-D Earth model and is usually associated with centroid depth uncertainties of the order of 15 km [*Vallée et al.*, 2010; *Duputel et al.*, 2012]. Global CMT corrects 1-D Earth synthetic seismograms using first-order path-averaged phase perturbations [*Dziewonski et al.*, 1992]. Although these corrections yield smaller location uncertainties, GCMT solutions are affected by an average bias of 5–8 km to greater depths [*Hjörleifsdóttir and Ekström*, 2010].

To determine a range of reasonable centroid depths and to get rid of uncertainty due to unaccounted 3-D structures, we perform CMT inversions for the main shock and $M_w \geq 5.0$ aftershocks based on a 3-D Earth

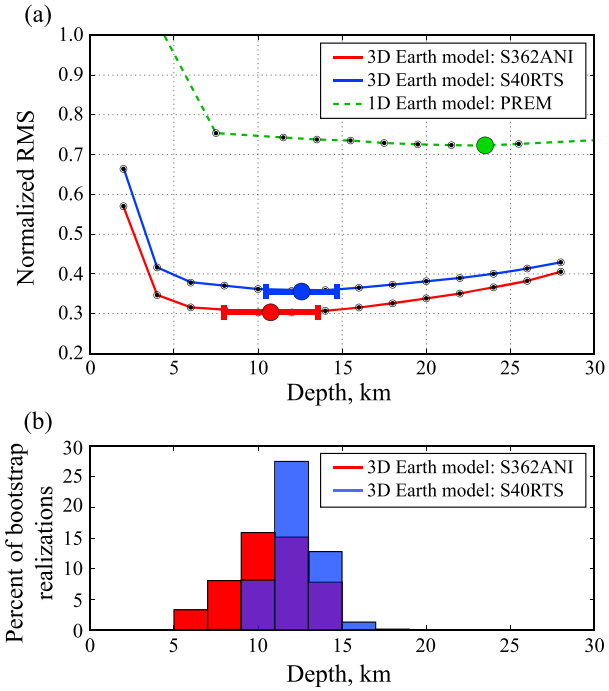

Figure 2. Centroid depth estimates in a 3-D Earth model for the 2015 Gorkha main shock. (a) Normalized RMS with respect to centroid depth. (b) Histogram of depth estimates from 5000 bootstrap realizations. Results are shown in red for S362ANI and in blue for S40RTS. Error bars in Figure 2a correspond to standard deviations estimated from 5000 bootstrap realizations presented in Figure 2b. Results obtained using the 1-D Earth model PREM are shown for reference in green.

model. The parameters to be determined are the elements of the seismic moment tensor as well as the centroid location and timing. At this stage, the horizontal coordinates of the centroid are fixed to the global CMT location, and the effect of finite-source duration is accounted for by assuming the moment rate function (MRF) to be an isosceles triangle (this hypothesis will be relaxed in the next section). Using an inversion procedure similar to *Duputel et al.* [2012], the centroid depth is estimated by grid searching the best point source location (minimizing the data misfit). The source duration and the centroid timing (i.e., the width and center of the triangular MRF) are evaluated using the same approach. The Green's functions are computed using the spectral-element method (SEM) [*Komatitsch and Tromp*, 1999] for a 3-D Earth model composed of S362ANI [*Kustowski et al.*, 2008] and Crust2.0 [*Bassin et al.*, 2000].

Our preferred CMT solutions for the main shock and $M_w \geq 5.0$ aftershocks are presented in Figure 1. These results are obtained using body waves and surface waves filtered between 80 and 200 s for $M_w \geq 6.0$ earthquakes and between 60 and 150 s for smaller events. We use a selected set of 139 broadband seismograms including 77 vertical and 62 horizontal components from global seismological networks. Being contaminated by large amplitude wave trains of the main shock and of the $M_w = 7.2$ aftershock, the $M_w \geq 6$ aftershocks on 25 April and 12 May are analyzed using a smaller data set, after careful selection of nondisturbed waveforms (cf. supporting information). The centroid depth grid search is presented in Figure 2 for the main shock and in Figure S2 for $M_w \geq 5$ aftershocks. For each explored depth, the normalized root-mean-square (RMS) misfit is computed using

$$\rho = \|\mathbf{s} - \mathbf{d}\|_2 / \|\mathbf{s}\|_2 \quad (1)$$

where **d** and **s** are, respectively, the data and synthetic traces. After grid search, all optimum centroid depths are between 8 km and 14 km. Observed and predicted waveforms computed for our preferred CMT solutions are presented in Figures S3–S11 in the supporting information.

To analyze the variability of these depth estimates, we perform bootstrapping analysis based on 5000 random resampling of the channels used in the inversion [*Efron and Tibshirani*, 1994]. The histograms in Figures 2 and S2 show the distribution of centroid depths estimated from these 5000 realizations. The number of random samples has been chosen to ensure stability of bootstrapping estimates. In practice, histograms of centroid depths are stable when using more than 1000 realizations. The bootstrap results indicate centroid depths shallower than 15 km (except for the 25 April aftershock associated with large uncertainty). These estimates are globally consistent with aftershock locations from *Adhikari et al.* [2015] shown in Figure 3d and relocations from *Bai et al.* [2016] showing that more than 65% of aftershocks occurred at depth between 10 and 15 km. Such bootstrap analysis does not fully capture the uncertainty due to inaccuracies in the Earth model used to compute the Green's functions. To investigate this effect, Figure 2 shows the result of

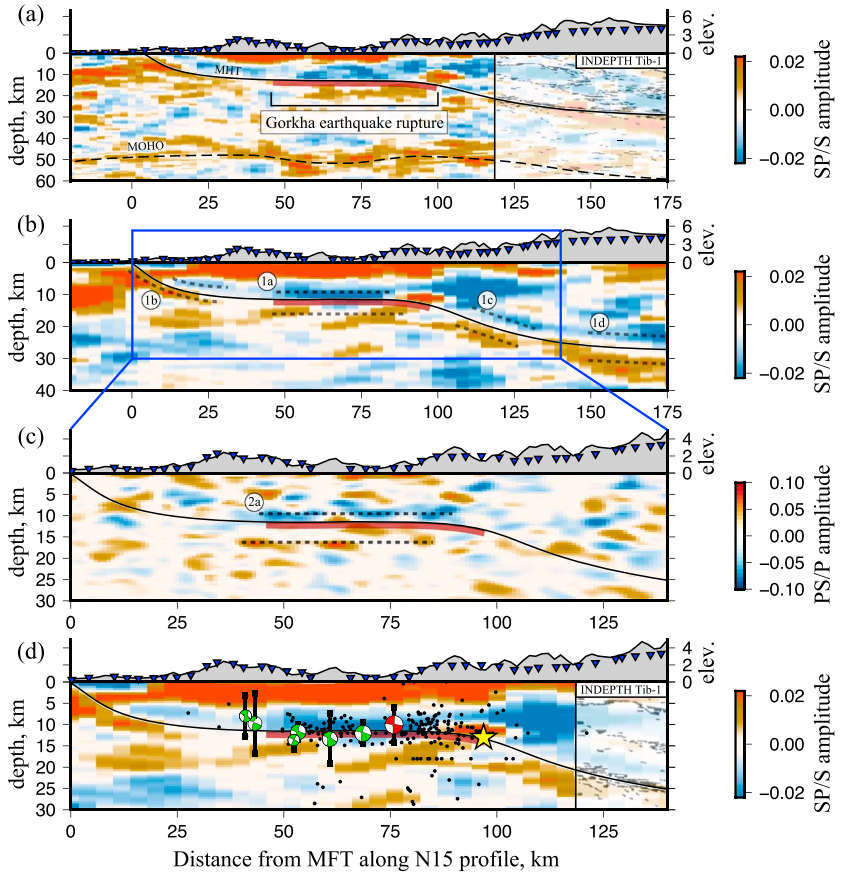

Figure 3. Imaging the Main Himalayan Thrust. (a) *S*-to-*P* receiver function migration image in the 0.2–2 Hz passband showing MHT and Moho. (b) *S*-to-*P* receiver function migration image in the 0.2–5 Hz passband. (c) *P*-to-*S* receiver function migration image. (d) Seismicity over the *S*-to-*P* image (also shown in Figure 3b).Back hemisphere focal mechanisms for the main shock (in red) and largest aftershocks (in green) are obtained from CMT inversion using 3-D SEM Green's functions. Dashed black lines and circles with letters mark features discussed in the main text. Black line shows our interpretation of the MHT geometry. Yellow star indicates the hypocenter of the main shock from USGS projected on the MHT interface. Black dots are aftershocks from *Adhikari et al.* [2015] within +/−40 km of the Hi-CLIMB profile. Blue triangles are station locations. The right inset in Figures 3a and 3d corresponds to the INDEPTH Tib-1 reflection profile [*Hauck et al.*, 1998] presented at matching distance from the MFT. Notice that the Tib-1 profile has a different orientation and is located about 400 km east of the Hi-CLIMB profile. Raw receiver function images are also presented in Figures S13 and S14 available in the supporting information.

the centroid depth grid search for the main shock by replacing S362ANI with S40RTS [*Ritsema et al.*, 2011]. The inversion results obtained using both models are quite similar with $M_w \sim 7.8$, dip ~ 7°, and depth ~ 12 km. S40RTS is associated with slightly larger RMS misfits but with smaller variability in bootstrapped depth estimates. The depth grid search performed using the 1-D Earth model preliminary reference Earth model (PREM) [*Dziewonski and Anderson*, 1981] is also shown for reference. Since fundamental mode surface waves are sensitive to shallow structures, PREM is associated with larger misfit and leads to a larger depth of ~23 km. Our CMT analysis being based on long-period surface waves, the computed Green's functions, must account for crustal heterogeneities but also incorporate effects of deeper structures in the upper mantle. This is illustrated in Figure S12, showing that records are poorly predicted by a model composed of Crust2.0 over a 1-D mantle contrarily to a full 3-D model.

In parallel to long-period CMT inversions, we reinvestigated the receiver functions from the Hi-CLIMB experiment [*Nabelek et al.*, 2009] in order to compare centroid locations with major crustal impedance contrasts. The Hi-CLIMB stations were operated between 2002 and 2004 and were located along a N15°E oriented profile that runs on top of the rupture area of the Gorkha earthquake (Figure 1). We process both *P*-to-*S* (PS) and *S*-to-*P* (SP) RFs from a selection of teleseismic events with magnitude $M_w \geq 5.8$ using an iterative time domain

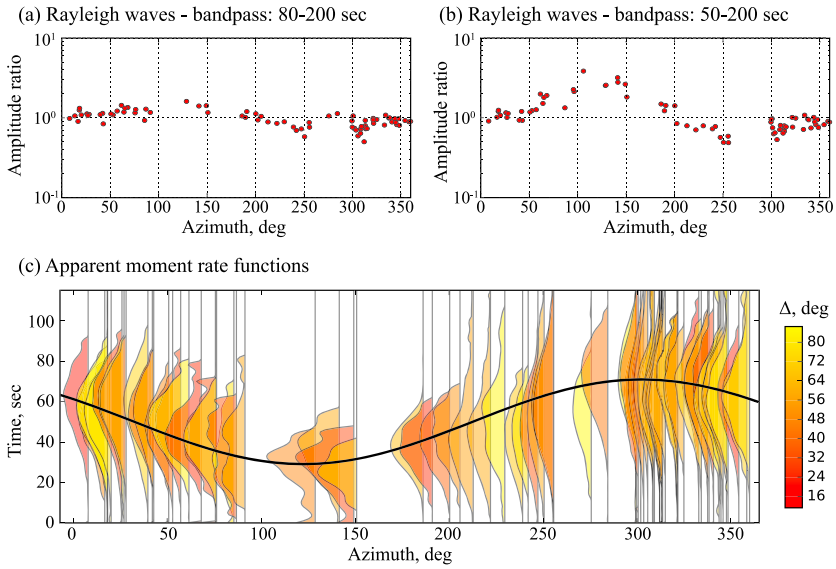

Figure 4. Directivity effects. Rayleigh wave amplitude ratios are shown using different passbands. (a) Amplitude ratios between 80 and 200 s. (b) Ratios between 50 and 200 s. Directivity effects are particularly visible when short periods are included. (c) Apparent moment rate functions are shown as a function of azimuth and colored by epicentral distance. These represent seismic moment as a function of time observed at different stations. The black curve corresponds to the centroid location, showing the predicted arrival time of energy radiated from this location (see yellow circle in Figure 1).

deconvolution approach [*Ligorria and Ammon*, 1999]. RF migration is performed using the common conversion point technique [*Dueker and Sheehan,* 1998; *Zhu*, 2000] and the 1-D velocity model for Nepal from *Grandin et al.* [2015]. To attain the best possible resolution in the shallow part of the MHT, seismograms are filtered in the 0.5–2 Hz passband for PS-RFs and in the 0.2–5 Hz and 0.2–2 Hz passbands for SP-RFs. The main advantage of SP-RFs compared to PS-RFs is that they are free from crustal reverberations that can contaminate PS-RFs cross sections.

SP and PS migrations are presented in Figures 3, S13, and S14. Between 40 km and 90 km north of the MFT, the images show a marked negative impedance contrast at ~10 km depth followed by a broader positive contrast at a depth of ~15 km (1a and 2a in Figure 3). These features being consistent on both SP and PS images, we are confident that they correspond to a quasi horizontal LVZ below Nepal and also are visible on the shallow portion of the broader sections of *Nabelek et al.* [2009] and *Wittlinger et al.* [2009] and along other profiles crossing the Himalayas [*Schulte-Pelkum et al.,* 2005; *Caldwell et al.,* 2013] but generally not providing such a high resolution as the RF images presented here. Comparison with centroid depths of the Gorkha earthquake sequence in Figure 3d confirms that this LVZ corresponds to the receiver function signature of the MHT. Interestingly, we also notice that the horizontal extent of the LVZ seems to match the along dip distribution of coseismic slip and the aftershock epicenters [*Adhikari et al.*, 2015; *Bai et al.*, 2016].

In addition to the horizontal LVZ, the SP cross sections presented in Figures 3a, 3b, S13, and S14 show several features. (i) A shallow ~20° north dipping weak negative impedance over a positive contrast at 0–30 km from the MFT (1b in Figure 3b, also visible in Figure 3a). (ii) A ~17° dipping structure at 100–130 km of the MFT (1c in Figure 3) connecting the horizontal LVZ with (iii) a deeper, subhorizontal LVZ at distances larger than 140 km (1d in Figure 3). These features are interpreted here as receiver function signatures of the MHT outlined with a black line in Figures 3 and S14. The southernmost feature (1b) likely corresponds to the shallow ramp at the MFT found in several geological cross sections [e.g., *Lavé and Avouac*, 2000] or the base of underthrusted Ganges sediments below the MHT. The northern deep structure (1d) corresponds to the deeper part of the MHT and is consistent both with the northern midcrustal LVZ segment observed by *Nabelek et al.* [2009] and with the International Deep Profiling of Tibet and the Himalaya (INDEPTH) Tib-1 seismic profile (shown in Figures 3a and 3d) [*Hauck et al.*, 1998]. The intermediate dipping structure (1c) is consistent with the midcrustal MHT ramp mentioned in previous geological reconstructions [e.g., *Lavé and Avouac*, 2001] and suggested by joint analysis of interseismic and coseismic geodetic observations [*Elliott et al.*, 2016].

3. Surface Wave Directivity

To investigate possible rupture directivity effects visible at long period for the $M_w = 7.8$ Nepal earthquake, we measure the ratio between observed and predicted surface wave amplitudes in the 50–200 s and 80–200 s passbands. The effect of radiation pattern, dispersion, and attenuation are removed using single-point-source synthetic SEM seismograms computed for the optimum CMT solution obtained in the previous section. We focus here on the variation of the amplitude ratio (observed/predicted) as a function of azimuth. We use minor-arc Rayleigh waves (R1) which provides relatively good azimuthal coverage for epicentral distances $\Delta < 90°$. If directivity effects are negligible, the observed/predicted amplitude ratios would be unity for all azimuths. For the $M_w = 7.8$ Nepal earthquake, we clearly see in Figures 4a and 4b that the Rayleigh wave amplitudes are enhanced in azimuths around N120°E. The directivity effects are stronger at shorter period (i.e., in Figure 4b), in agreement with what one would expect for a rupture with unilateral propagation toward east-southeast [*Ben-Menahem*, 1961; *Haskell*, 1963].

We also compute apparent Rayleigh wave moment rate functions (MRFs) to extract long-period finiteness observables. The dispersive wave-propagation effects are removed by deconvolving the data by point-source synthetic seismograms computed from our preferred CMT solution in section 2. We use broadband (periods of 10–200 s) SEM synthetics computed for a 3-D Earth model (S362ANI and Crust2.0). We use the projected Landweber deconvolution method [*Bertero et al.*, 1999; *Lanza et al.*, 1999] imposing causality, positivity, and a maximum rupture duration of 100 s. The MRFs are shown in Figure 4c. Azimuthal variation in apparent duration and peak MRF amplitude is clearly visible. This directivity effect is consistent with unilateral rupture propagation toward east-southeast as suggested by amplitude ratios and the location of the centroid relative to the hypocenter (cf. yellow star and yellow circle in Figure 1). To study this apparent directivity, we image the spatial distribution of long-period seismic wave radiation. To do so, the MRFs are averaged in 10° azimuthal windows and back projected over a gridded region around the $M_w = 7.8$ epicenter assuming an average phase velocity of 4.0 km/s. The resulting peak stacked amplitude, shown in Figure 1, provides an image of where long-period radiation emanated from the source region (darker colors indicate stronger long-period source radiation). This suggests a fairly simple rupture process with a primary source of long-period energy concentrated in the area north of Kathmandu.

4. Discussion and Conclusion

To resolve the geometry of the MHT below central Nepal, we performed a joint analysis of CMT solutions for the 2015 Gorkha sequence and receiver functions from the Hi-CLIMB experiment. We conducted long-period CMT inversions using SEM Green's functions for 3-D Earth models. We also processed both PS and SP receiver functions to enable high-resolution imaging below Lesser and Higher Himalayas. Below Nepal, this analysis confirmed the presence of a LVZ at 10–15 km depth as reported previously by *Nabelek et al.* [2009]. On the other hand, our CMT analysis revealed that the Gorkha main shock and $M_w \geq 5.0$ aftershocks occurred at depths ranging between 8 km and 14 km, which clearly show that the flat portion of MHT is located within the LVZ revealed by receiver function analysis. Other observations of such LVZ has been reported along other profiles crossing the Himalayas [*Schulte-Pelkum et al.*, 2005; *Caldwell et al.*, 2013] indicating that the geometry and receiver function signature of the MHT is similar along the Himalayan front. On a larger scale, SP receiver function migration outlines the ramp-flat-ramp geometry of the MHT, with a shallow thrust fault flattening at depths between 10 and 15 km followed by a midcrustal ramp connecting to a deeper low-dipping thrust at depths larger than 25 km.

Reconciling the subhorizontal portion of the ruptured area of the MHT as imaged by the LVZ with the ~7° dip of our CMT solution for the Gorkha earthquake requires that this event also ruptured a steeper part of the MHT presumably corresponding to the upper end of the midcrustal ramp. This interpretation is consistent with the main shock hypocenter located on the updip edge of the crustal ramp as shown in Figure 3d. The existence of this steeper thrust also agrees with previous geological, geodetic, and geomorphological studies and may play a strong role on the uplift of the high Himalaya as advocated by *Elliott et al.* [2016]. At distances larger than 130 km from the MFT this steep thrust roots into a lower dipping LVZ having a thickness of 5 to 10 km in our SP images that can be interpreted as the aseismic shear zone discussed in previous studies [e.g., *Cattin and Avouac*, 2000].

To further interpret our image of the LVZ in the subhorizontal portion of the MHT, we designed a simple velocity model able to fit both SP and PS receiver functions in this region (cf. Text S1 in the supporting information). Our preferred model presented in Figure S16 includes a sharp ~10% shear velocity decrease at ~10 km

depth followed by a smooth velocity recovery. Such a sharp velocity decrease clearly reinforces previous hypotheses suggesting the existence of fluids released by dewatering of underthrust sediments around the flat portion of the MHT [*Nabelek et al.*, 2009]. This interpretation is in good agreement with high conductivity features revealed by magnetotelluric studies [*Lemonnier et al.*, 1999; *Patro and Harinarayana*, 2009] and with temperature conditions inferred from thermokinematic modeling [*Bollinger et al.*, 2006; *Hetényi et al.*, 2007]. Whether the MHT corresponds to the negative impedance contrast at ~10 km depth or to the broader positive impedance contrast between 15 and 20 km is unsure since the vertical resolution of receiver functions is about 2 km. However, we favor the hypothesis that the MHT lies between 10 and 15 km, where the seismic velocity is the lowest and where most earthquakes occur. The spreading of aftershocks within the LVZ might correspond to uncertainties in depth estimates but may also be due to the occurrence of aftershocks on subfaults surrounding the MHT. As discussed in *Bai et al.* [2016], the ~25° dip angle of some small aftershocks suggests that some events might occur on steeper faults in the hanging wall. The activation of such steeper faults during the Gorkha earthquake sequence remains however uncertain as dip angle estimates are affected by the moment-dip trade-off for shallow thrust events [*Tsai et al.*, 2011].

Our long-period analysis of the $M_w = 7.8$ Gorkha earthquake indicates a simple unilateral rupture propagation toward east-southeast. MRF backprojection shows that long-period seismic energy mainly emanated in the north of Kathmandu, in agreement with preliminary finite-fault models [*Avouac et al.*, 2015; *Galetzka et al.*, 2015; *Grandin et al.*, 2015; *Yagi and Okuwaki*, 2015; *Elliott et al.*, 2016]. High-frequency radiators revealed by backprojection results are located downdip of these long-period radiation sources [*Avouac et al.*, 2015; *Fan and Shearer*, 2015; *Grandin et al.*, 2015]. Although the spatial resolution is lower than short-period *P* wave backprojections, imaging long-period seismic energy provides a good indication of seismic moment distribution independent of any assumption on the fault geometry [*Yue et al.*, 2012]. These observations suggest similar behavior as subduction zone earthquakes, where high-frequency sources are distributed at the downdip edge of the seismogenic domain, which is usually interpreted as variations in frictional and stress heterogeneity with depth [*Huang et al.*, 2012; *Lay et al.*, 2012]. In addition, the location of high-frequency sources matches the position of the hinge line between the flat and the deeper ramp that also marks the transition zone between locked and stable sliding portions of the MHT [*Ader et al.*, 2012]. As discussed by *Denolle et al.* [2015] and *Elliott et al.* [2016], this suggests possible structural control on the generation of high-frequency energy.

The smooth rupture process in the updip part of the rupture with a depletion of high-frequency emissions can also be related to the presence of fluids revealed by the LVZ in receiver function images. As shown in Figure 3d, the horizontal extent of the LVZ seems to match the along-dip distribution of coseismic slip and aftershock epicenters. Such reverse polarities associated with elevated fluid pressures have been previously observed in shallow portions of subduction zones [*Bangs et al.*, 1996; *Park et al.*, 2002; *Tobin and Saffer*, 2009] and has been invoked to explain frequency-dependent rupture process of megathrust earthquakes such as the 2004 Sumatra-Andaman event [*Lay et al.*, 2012] or the 2011 Tohoku-oki event [*Huang et al.*, 2012]. Increase in fluid pressure results in a local decrease of the effective normal stress and is often associated with a depletion of high-frequency emissions [*Ito and Obara*, 2006; *Lengliné et al.*, 2014]. Elevated pore fluid pressure due to sediment dewatering might therefore explain the frequency-dependent rupture process observed for the Gorkha event, with a smooth updip rupture process causing moderate peak ground acceleration in Kathmandu. Whether such phenomenon is present in most subduction megathrusts is not yet established and other parameters such as temperature and fault geometry might also affect rupture behavior. Full quantification of mechanisms governing depth-varying seismic characteristics and along-dip segmentation of megathrust faults is an important challenge for the future and has important impacts on seismic hazard assessment.

Acknowledgments

This research was supported by the Initiative d'Excellence (IDEX) funding framework (Université de Strasbourg), the Institut National des Sciences de l'Univers (INSU), and the CNRS international program for scientific cooperation (PICS). The research described herein used data from various global networks (including II, IU, G, and GE) and from the first phase of the Hi-CLIMB experiment (doi: 10.7914/SN/XF_2002). All used data are available through the IRIS DMC. We are grateful to the operators of these networks for ensuring the high quality of the data and making them publicly available. We thank R. Jolivet, H. Yue, J. Van der Woerd, and C. Satriano for helpful discussions. We thank the Editor, J. Ritsema, and two anonymous reviewers for their constructive comments, which helped improve this manuscript.

References

Ader, T., et al. (2012), Convergence rate across the Nepal Himalaya and interseismic coupling on the Main Himalayan Thrust: Implications for seismic hazard, *J. Geophys. Res.*, *117*, B04403, doi:10.1029/2011JB009071.

Adhikari, L. B., et al. (2015), The aftershock sequence of the 2015 April 25 Gorkha–Nepal earthquake, *Geophys. J. Int.*, *203*(3), 2119–2124.

Avouac, J.-P., L. Meng, S. Wei, T. Wang, and J.-P. Ampuero (2015), Lower edge of locked Main Himalayan Thrust unzipped by the 2015 Gorkha earthquake, *Nat. Geosci.*, doi:10.1038/ngeo2518.

Bai, L., H. Liu, J. Ritsema, J. Mori, T. Zhang, Y. Ishikawa, and G. Li (2016), Faulting structure above the Main Himalayan Thrust as shown by relocated aftershocks of the 2015 Mw7.8 Gorkha, Nepal, earthquake, *Geophys. Res. Lett.*, *43*, 637–642, doi:10.1002/2015GL066473.

Bangs, N. L., T. H. Shipley, and G. F. Moore (1996), Elevated fluid pressure and fault zone dilation inferred from seismic models of the northern Barbados Ridge decollement, *J. Geophys. Res.*, *101*(B1), 627–642.

Bassin, C., G. Laske, and G. Masters (2000), The current limits of resolution for surface wave tomography in North America, *Eos Trans. AGU*, *81*, F897.
Ben-Menahem, A. (1961), Radiation of seismic surface-waves from finite moving sources, *Bull. Seismol. Soc. Am.*, *51*, 401–435.
Bertero, M., D. Bindi, P. Boccacci, M. Cattaneo, C. Eva, and V. Lanza (1999), Application of the projected Landweber method to the estimation of the source time function in seismology, *Inverse Prob.*, *13*(2), 465–486, doi:10.1088/0266-5611/13/2/017.
Bilham, R. (1995), Location and magnitude of the 1833 Nepal Earthquake and its relation to the rupture zones of Contiguous Great Himalayan Earthquakes, *Curr. Sci.*, *69*(2), 101–128.
Bollinger, L., J. P. Avouac, O. Beyssac, E. J. Catlos, T. M. Harrison, M. Grove, et al. (2004), Thermal structure and exhumation history of the Lesser Himalaya in central Nepal, *Tectonics*, *23*, TC5015, doi:10.1029/2003TC001564.
Bollinger, L., P. Henry, and J. Avouac (2006), Mountain building in the Nepal Himalaya: Thermal and kinematic model, *Earth Planet. Sci. Lett.*, *244*(1–2), 58–71, doi:10.1016/j.epsl.2006.01.045.
Bollinger, L., S. N. Sapkota, P. Tapponnier, Y. Klinger, M. Rizza, J. Van der Woerd, D. R. Tiwari, R. Pandey, A. Bitri, and S. B. de Berc (2014), Estimating the return times of great Himalayan earthquakes in eastern Nepal: Evidence from the Patu and Bardibas strands of the Main Frontal Thrust, *J. Geophys. Res. Solid Earth*, *119*, 7123–7163, doi:10.1002/2014JB010970.
Brown, L. D., W. Zhao, K. D. Nelson, M. Hauck, D. Alsdorf, A. Ross, M. Cogan, M. Clark, X. Liu, and J. Che (1996), Bright spots, structure, and magmatism in southern Tibet from INDEPTH seismic reflection profiling, *Science*, *274*(5293), 1688–1690, doi:10.1126/science.274.5293.1688.
Brunel, M. (1986), Ductile thrusting in the Himalayas: Shear sense criteria and stretching lineations, *Tectonics*, *5*(2), 247–265, doi:10.1029/TC005i002p00247.
Caldwell, W. B., S. L. Klemperer, J. F. Lawrence, S. S. Rai, and Ashish (2013), Characterizing the Main Himalayan Thrust in the Garhwal Himalaya, India with receiver function CCP stacking, *Earth Planet. Sci. Lett.*, *367*, 15–27.
Cattin, R., and J. P. Avouac (2000), Modeling mountain building and the seismic cycle in the Himalaya of Nepal, *J. Geophys. Res.*, *105*, 13,389–13,407, doi:10.1029/2000JB900032.
Denolle, M. A., W. Fan, and P. M. Shearer (2015), Dynamics of the 2015 *M*7.8 Nepal earthquake, *Geophys. Res. Lett.*, *42*, 7467–7475, doi:10.1002/2015GL065336.
Dueker, K. G., and A. F. Sheehan (1998), Mantle discontinuity structure beneath the Colorado Rocky Mountains and High Plains, *J. Geophys. Res.*, *103*(B4), 7153–7169, doi:10.1029/97JB03509.
Duputel, Z., L. Rivera, H. Kanamori, and G. Hayes (2012), *W* phase source inversion for moderate to large earthquakes (1990–2010), *Geophys. J. Int.*, *189*(2), 1125–1147, doi:10.1111/j.1365-246X.2012.05419.x.
Duputel, Z., P. S. Agram, M. Simons, S. E. Minson, and J. L. Beck (2014), Accounting for prediction uncertainty when inferring subsurface fault slip, *Geophys. J. Int.*, *197*(1), 464–482, doi:10.1093/gji/ggt517.
Dziewonski, A. M., and D. L. Anderson (1981), Preliminary reference Earth model, *Phys. Earth Planet. Inter.*, *25*(4), 297–356, doi:10.1016/0031-9201(81)90046-7.
Dziewonski, A. M., G. Ekström, and M. P. Salganik (1992), Centroid-moment tensor solutions for July–September 1991, *Phys. Earth Planet. Inter.*, *72*(1–2), 1–11.
Elliott, J. R., R. Jolivet, P. J. González, J. P. Avouac, J. Hollingsworth, M. P. Searle, and V. L. Stevens (2016), Himalayan megathrust geometry and relation to topography revealed by the Gorkha earthquake, *Nat. Geosci.*, doi:10.1038/ngeo2623.
Efron, B., and R. J. Tibshirani (1994), *An Introduction to the Bootstrap*, Monographs on Statistics Applied Probability, Chapman and Hall/CRC, New York.
Ekström, G., M. Nettles, and A. M. Dziewonski (2012), The global CMT project 2004–2010: Centroid-moment tensors for 13,017 earthquakes, *Phys. Earth Planet. Inter.*, *200–201*, 1–9.
Fan, W., and P. M. Shearer (2015), Detailed rupture imaging of the 25 April 2015 Nepal earthquake using teleseismic Pwaves, *Geophys. Res. Lett.*, *42*, 5744–5752, doi:10.1002/2015GL064587.
Galetzka, J., et al. (2015), Slip pulse and resonance of Kathmandu basin during the 2015 M_w 7.8 Gorkha earthquake, Nepal imaged with geodesy, *Science*, doi:10.1126/science.aac6383.
Geller, R., and H. Kanamori (1977), Magnitudes of great shallow earthquakes from 1904 to 1952, *Bull. Seismol. Soc. Am.*, *67*, 587–598.
Grandin, R., M. Vallée, C. Satriano, R. Lacassin, Y. Klinger, M. Simoes, and L. Bollinger (2015), Rupture process of the M_w = 7.9 2015 Gorkha earthquake (Nepal): Insights into Himalayan megathrust segmentation, *Geophys. Res. Lett.*, *42*, 8373–8382, doi:10.1002/2015GL066044.
Haskell, N. A. (1963), Radiation pattern of Rayleigh waves from a fault of arbitrary dip and direction of motion in a homogeneous medium, *Bull. Seismol. Soc. Am.*, *53*, 619–642.
Hauck, M. L., K. D. Nelson, L. D. Brown, W. Zhao, and A. R. Ross (1998), Crustal structure of the Himalayan orogen at ~ 90° east longitude from Project INDEPTH deep reflection profiles, *Tectonics*, *17*(4), 481–500, doi:10.1029/98TC01314.
Hetényi, G., R. Cattin, F. Brunet, L. Bollinger, J. Vergne, J. L. Nábělek, and M. Diament (2007), Density distribution of the India plate beneath the Tibetan plateau: Geophysical and petrological constraints on the kinetics of lower-crustal eclogitization, *Earth Planet. Sci. Lett.*, *264*(1–2), 226–244.
Hjörleifsdóttir, V., and G. Ekström (2010), Effects of tree-dimensional Earth structure on CMT earthquake parameters, *Phys. Earth Planet. Inter.*, *179*, 178–190.
Huang, Y., L. Meng, and J.-P. Ampuero (2012), A dynamic model of the frequency-dependent rupture process of the 2011 Tohoku-Oki earthquake, *Earth Planets Space*, *64*(12), 1061–1066.
Ito, Y., and K. Obara (2006), Very low frequency earthquakes within accretionary prisms are very low stress-drop earthquakes, *Geophys. Res. Lett.*, *33*, L09302, doi:10.1029/2006GL025883.
Komatitsch, D., and J. Tromp (1999), Introduction to the spectral element method for three-dimensional seismic wave propagation, *Geophys. J. Int.*, *139*(3), 806–822.
Kustowski, B., G. Ekström, and A. M. Dziewonski (2008), Anisotropic shear-wave velocity structure of the Earth's mantle: A global model, *J. Geophys. Res.*, *113*, B06306, doi:10.1029/2007JB005169.
Lanza, V., D. Spallarossa, M. Cattaneo, D. Bindi, and P. Augliera (1999), Source parameters of small events using constrained deconvolution with empirical Green's functions, *Geophys. J. Int.*, *137*(3), 651–662.
Lavé, J., and J. P. Avouac (2000), Active folding of fluvial terraces across the Siwaliks Hills, Himalayas of central Nepal, *J. Geophys. Res.*, *105*(B3), 5735–5770, doi:10.1029/1999JB900292.
Lavé, J., and J. P. Avouac (2001), Fluvial incision and tectonic uplift across the Himalayas of central Nepal, *J. Geophys. Res.*, *106*(B11), 26,561–26,591, doi:10.1029/2001JB000359.
Lay, T., H. Kanamori, C. J. Ammon, K. D. Koper, A. R. Hutko, L. Ye, H. Yue, and T. M. Rushing (2012), Depth-varying rupture properties of subduction zone megathrust faults, *J. Geophys. Res.*, *117*, B04311, doi:10.1029/2011JB009133.

Lengliné, O., L. Lamourette, L. Vivin, N. Cuenot, and J. Schmittbuhl (2014), Fluid-induced earthquakes with variable stress drop, *J. Geophys. Res. Solid Earth*, *119*, 8900–8913, doi:10.1002/2014JB011282.

Lemonnier, C., G. Marquis, F. Perrier, J. P. Avouac, G. Chitrakar, B. Kafle, S. Sapkota, U. Gautam, D. Tiwari, and M. Bano (1999), Electrical structure of the Himalaya of Central Nepal: High conductivity around the mid-crustal ramp along the MHT, *Geophys. Res. Lett.*, *26*(21), 3261–3264, doi:10.1029/1999GL008363.

Ligorria, J. P., and C. J. Ammon (1999), Iterative deconvolution and receiver-function estimation, *Bull. Seismol. Soc. Am.*, *89*(5), 1395–1400.

Nabelek, J., G. Hetényi, J. Vergne, S. Sapkota, B. Kafle, M. Jiang, H. Su, J. Chen, B. S. Huang, and T. H. C. Team (2009), Underplating in the Himalaya-Tibet collision zone revealed by the Hi-CLIMB experiment, *Science*, *325*(5946), 1371–1374.

Nakanishi, I., and H. Kanamori (1982), Effects of lateral heterogeneity and source process time on the linear moment tensor inversion of long-period Rayleigh waves, *Bull. Seismol. Soc. Am.*, *72*(6A), 2063–2080.

Park, J.-O., T. Tsuru, S. Kodaira, P. R. Cummins, and Y. Kaneda (2002), Splay fault branching along the Nankai Subduction Zone, *Science*, *297*(5584), 1157–1160.

Patro, P. K., and T. Harinarayana (2009), Deep geoelectric structure of the Sikkim Himalayas (NE India) using magnetotelluric studies, *Phys. Earth Planet. Inter.*, *173*(1–2), 171–176, doi:10.1016/j.pepi.2008.10.011.

Ritsema, J., A. Deuss, H. J. van Heijst, and J. H. Woodhouse (2011), S40RTS: A degree-40 shear-velocity model for the mantle from new Rayleigh wave dispersion, teleseismic traveltime and normal-mode splitting function measurements, *Geophys. J. Int.*, *184*(3), 1223–1236.

Sapkota, S. N., L. Bollinger, Y. Klinger, P. Tapponnier, Y. Gaudemer, and D. Tiwari (2013), Primary surface ruptures of the great Himalayan earthquakes in 1934 and 1255, *Nat. Geosci.*, *6*(1), 71–76, doi:10.1038/ngeo1669.

Schulte-Pelkum, V., G. Monsalve, A. Sheehan, M. R. Pandey, S. Sapkota, R. Bilham, and F. Wu (2005), Imaging the Indian subcontinent beneath the Himalaya, *Nature*, *435*(7046), 1222–1225.

Smith, G. P., and G. Ekström (1996), Improving teleseismic event locations using a three-dimensional earth model, *Bull. Seismol. Soc. Am.*, *86*(3), 788–796.

Tobin, H. J., and D. M. Saffer (2009), Elevated fluid pressure and extreme mechanical weakness of a plate boundary thrust, Nankai Trough subduction zone, *Geology*, *37*(8), 679–682.

Tsai, V. C., G. P. Hayes, and Z. Duputel (2011), Constraints on the long-period moment-dip tradeoff for the Tohoku earthquake, *Geophys. Res. Lett.*, *38*, L00G17, doi:10.1029/2011GL049129.

Vallée, M., J. Charléty, and A. Ferreira (2010), SCARDEC: A new technique for the rapid determination of seismic moment magnitude, focal mechanism and source time functions for large earthquakes using body-wave deconvolution, *Geophys. J. Int.*, *184*, 338–358.

Wittlinger, G., V. Farra, G. Hetényi, J. Vergne, and J. Nabelek (2009), Seismic velocities in Southern Tibet lower crust: A receiver function approach for eclogite detection, *Geophys. J. Int.*, *177*(3), 1037–1049.

Wobus, C., A. Heimsath, K. Whipple, and K. Hodges (2005), Active out-of-sequence thrust faulting in the central Nepalese Himalaya, *Nature*, *434*(7036), 1008–1011.

Yagi, Y., and R. Okuwaki (2015), Integrated seismic source model of the 2015 Gorkha, Nepal, earthquake, *Geophys. Res. Lett.*, *42*, 6229–6235, doi:10.1002/2015GL064995.

Yue, H., T. Lay, and K. D. Koper (2012), En echelon and orthogonal fault ruptures of the 11 April 2012 great intraplate earthquakes, *Nature*, *490*, 245–249.

Zhao, W., K. D. Nelson, J. Che, J. Quo, D. Lu, C. Wu, and X. Liu (1993), Deep seismic reflection evidence for continental underthrusting beneath southern Tibet, *Nature*, *366*(6455), 557–559.

Zhu, L. (2000), Crustal structure across the San Andreas Fault, southern California from teleseismic converted waves, *Earth Planet. Sci. Lett.*, *179*(1), 183–190.